Available online at www.sciencedirect.com
SCIENCE DIRECT®
Journal of Sound and Vibration 281 (2005) 119–139
JOURNAL OF SOUND AND VIBRATION
www.elsevier.com/locate/jsvi

Free vibration analysis of piezoelectric coupled thin and thick annular plate

W.H. Duan, S.T. Quek*, Q. Wang[1]

Department of Civil Engineering, National University of Singapore, 1 Engineering Drive 2, EIA-07-03, Singapore

Received 23 May 2003; accepted 12 January 2004
Available online 3 September 2004

Abstract

This paper presents the free vibration analysis of piezoelectric coupled annular plates using the Kirchhoff and Mindlin plate models. The distribution of electric potential along the thickness direction in the piezoelectric layer is simulated by a sinusoidal function such that the Maxwell static electricity equation is satisfied. The analytical solutions are derived and validated by comparing the resonant frequencies and mode shapes of the piezoelectric coupled annular plates with those obtained by finite element (FE) analysis. Mindlin model provides better solutions than those from Kirchhoff model and the deviation from FE results is larger for higher resonant frequencies. The piezoelectric layer increases the resonant frequencies, being more significant for thicker layers. The effect is smaller for higher modes and for smaller radius to thickness ratio of the plate. The analytical solutions and findings contribute towards a simplified model for the parametric study and understanding of vibration of piezoelectric-coupled annular plate, relevant to the design of ultrasonic motor.

1. Introduction

The study of embedded or surface-mounted piezoelectric materials in structures has received considerable attention in recent years because piezoelectric materials are more extensively used

*Corresponding author. Tel.: +65-6874-2263.
E-mail address: cveqst@nus.edu.sg (S.T. Quek).
[1]Current address: Department of Mechanical, Materials and Aerospace Engineering, University of Central Florida, Orlando, FL 32816-2450, USA.

0022-460X/$ - see front matter © 2004 Elsevier Ltd. All rights reserved.
doi:10.1016/j.jsv.2004.01.009

either as actuators or sensors. In order to effectively utilize the piezoelectric effect and actuating properties of piezoelectric materials, the interaction between the host structure and piezoelectric patch must be well understood. Ding et al. [1] obtained the general solutions for the dynamic equations of a transversely isotropic piezoelectric medium. Chen [2] simplified the equations of motion of a spherically isotropic elastic medium with radial inhomogeneity by adopting three displacement functions and considered some vibration problems of spherical shells. The mathematical analyses based on elastic theory were well conducted. Sun and Zhang [3] and Zhang and Sun [4] presented their research on the analysis of a sandwich beam and plate structure containing a piezoelectric core, where an electric field in the thickness direction may generate shear deformation within the core. Models for composite structures with piezoelectric materials as sensors and actuators have also been published [5,6]. In the latter addressing the mechanics model for the analysis of the coupled structure, the distribution of the electric potential is assumed to be uniform in the longitudinal direction of the piezoelectric actuator and linear in its thickness direction, which may violate Maxwell static electricity equation. Wang et al. [7] and Liu et al. [8] presented their research on the free vibration of piezoelectric sandwich thin and thick circular plates, respectively. Their hypotheses that the distribution of electric potential along the thickness direction in the piezoelectric layer is simulated by a sinusoidal function were validated by FE analysis and analytical solutions satisfying Maxwell static electricity equation were presented.

One of the significant applications of piezoelectric materials is the design of ultrasonic motor which was developed in early 1980s in response to the need for a lightweight, high-torque and low-speed motor for fractional horsepower applications. It is based on the concept of driving a rotor by mechanical vibration excited by piezoelectric patch on a stator via the piezoelectric effect [9]. The stator is usually modeled as a surface-mounted annular plate making use of its geometric property [10]. Takano et al. [10], Hagedorn and Wallashek [11], Yang and Que [12] and Friend and Stutts [13] studied the dynamics of an annular piezoelectric motor stator based on the thin annular plate model where shear deformation and rotary inertia was neglected. However, piezoelectric-coupled effect and the laminated nature of the stator have not been modeled completely in their studies. An analytical model of ultrasonic motor has been proposed by Hagood and McFarland [14] for the case of a laminated annular thin plate with clamped boundary conditions at the inner edge and free boundary conditions at the outer edge. They assumed that the distribution of electric potential is uniform in the thickness direction but Maxwell equation is not satisfied. Hence, there may be a need to provide a more accurate model to fully study the coupled piezoelectric effect.

In the present work, through transformation of variable suggested by Mindlin [15], analytical solutions for the free vibration of piezoelectric coupled annular plate based on Kirchhoff plate model (otherwise known as classical plate theory, or in short, CPT) and Mindlin plate model (also known as improved plate theory or IPT) have been presented. Sinusoidal function [7] is used to describe the distribution of electric potential along the thickness direction of thin and thick plate. Maxwell static electricity equation is included as one of the governing equations. Numerical investigations are performed for annular plates bonded by two piezoelectric layers and the results are verified against three-dimensional finite element (3D FE) analysis using ABAQUS Version 6.3. The applicability of the proposed model is analyzed by studying the effect of different thickness ratios of piezoelectric layer to host plate on the vibration of annular plate.

2. Strain and stress components in piezoelectric sandwich plate

Fig. 1 shows the cross section of a laminated annular plate consisting of one host layer and two piezoelectric layers. Both top and bottom surfaces of each piezoelectric layer are fully covered by electrodes that are shortly connected. The cylindrical coordinate system is adopted where the r–θ plane is coincident with the mid-plane of the undeformed plate. For such plate structures, the bending and twisting moments, and the transverse shearing forces (all in per unit of length) are defined in the customary manner

$$(M_{rr}, M_{\theta\theta}, M_{r\theta}) = \int (\sigma_{rr}, \sigma_{\theta\theta}, \tau_{r\theta}) z \, dz$$

$$(Q_r, Q_\theta) = \int (\tau_{rz}, \tau_{\theta z}) z \, dz \tag{1a, b}$$

where $\sigma_{rr}, \sigma_{\theta\theta}$ are normal stress components, and $\tau_{r\theta}$, τ_{rr}, $\tau_{\theta z}$ are shear stress components in the plate.

The kinematic fields in the host plate and piezoelectric layer are given by

$$\varepsilon_{rr} = \frac{\partial u_r}{\partial r},$$

$$\varepsilon_{\theta\theta} = \frac{u_r}{r} + \frac{\partial u_\theta}{r \partial \theta},$$

$$\gamma_{r\theta} = \frac{\partial u_r}{r \partial \theta} + \frac{\partial u_\theta}{\partial r} - \frac{u_\theta}{r},$$

$$\gamma_{rz} = \frac{\partial u_r}{\partial z} + \frac{\partial u_z}{\partial r},$$

$$\gamma_{\theta z} = \frac{\partial u_\theta}{\partial z} + \frac{\partial u_z}{r \partial \theta}, \tag{2a–e}$$

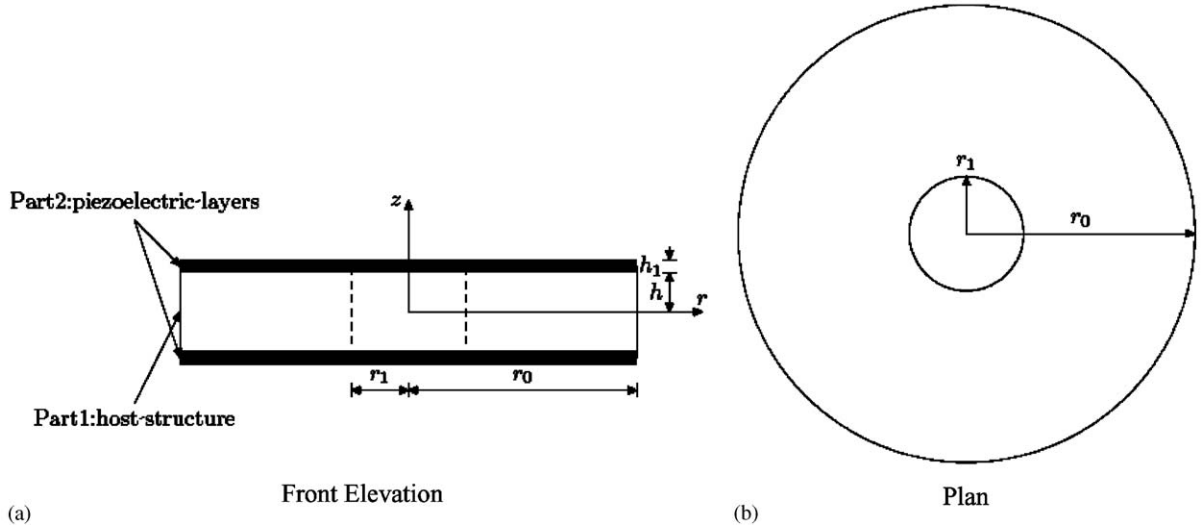

Fig. 1. Annular plate surface mounted with two piezoelectric layers.

where u_z, u_r, and u_θ are the displacements in the transverse, radial and tangential direction of the plate, respectively.

The constitutive relations in the host plate are expressed as

$$\begin{aligned}
\sigma_{rr}^h &= \frac{E}{1-\mu^2}(\varepsilon_{rr}+\mu\varepsilon_{\theta\theta}),\\
\sigma_{\theta\theta}^h &= \frac{E}{1-\mu^2}(\varepsilon_{\theta\theta}+\mu\varepsilon_{rr}),\\
\tau_{r\theta}^h &= \frac{E}{2(1+\mu)}\gamma_{r\theta},\\
\tau_{rz}^h &= \frac{E\kappa^2}{2(1+\mu)}\gamma_{rz},\\
\tau_{\theta z}^h &= \frac{E\kappa^2}{2(1+\mu)}\gamma_{\theta z},
\end{aligned} \tag{3a–e}$$

where the superscript h represents the variables in the host structure, E and μ are the Young's modulus and Poisson ratio of the host material, and κ is the shear factor in Mindlin plate model [15] to correct for the shear modulus, chosen as $\pi/\sqrt{12}$ here.

The constitutive relations in the piezoelectric layer are written as

$$\begin{aligned}
\sigma_{rr}^E &= \bar{C}_{11}^E\varepsilon_{rr}+\bar{C}_{12}^E\varepsilon_{\theta\theta}-\bar{e}_{31}E_z,\\
\sigma_{\theta\theta}^E &= \bar{C}_{12}^E\varepsilon_{rr}+\bar{C}_{11}^E\varepsilon_{\theta\theta}-\bar{e}_{31}E_z,\\
\tau_{r\theta}^E &= \tfrac{1}{2}(\bar{C}_{11}^E-\bar{C}_{12}^E)\gamma_{r\theta},\\
\tau_{rz}^E &= \kappa^2 C_{55}^E\gamma_{rz}+e_{15}E_r,\\
\tau_{\theta z}^E &= \kappa^2 C_{55}^E\gamma_{\theta z}+e_{15}E_\theta,
\end{aligned} \tag{4a–e}$$

where the superscript E represents the variables in the piezoelectric material; $\bar{C}_{11}^E$, $\bar{C}_{12}^E$ and $\bar{e}_{31}$ are the reduced material constants of the piezoelectric medium for plane stress problems given by $\bar{C}_{11}^E = C_{11}^E-(C_{13}^E)^2/C_{33}^E$, $\bar{C}_{12}^E = C_{12}^E-(C_{13}^E)^2/C_{33}^E$ and $\bar{e}_{31} = e_{31}-C_{11}^E e_{33}/C_{33}^E$; C_{11}^E, C_{12}^E, C_{13}^E, C_{33}^E and C_{55}^E are the moduli of elasticity under constant electric field, e_{31}, e_{33} and e_{15} are the piezoelectric constants, and E_z, E_r and E_θ are the electric field intensities in the radial, tangential and transverse direction, respectively. The latter are given by

$$\begin{aligned}
E_r &= -\frac{\partial\phi}{\partial r},\\
E_\theta &= -\frac{\partial\phi}{r\partial\theta},\\
E_z &= -\frac{\partial\phi}{\partial z},
\end{aligned} \tag{5a–c}$$

where ϕ is the electric potential at any point of the piezoelectric layers. The corresponding electric displacements D_r, D_θ and D_z are given by

$$\begin{aligned} D_r &= e_{15}\gamma_{rz} + \Xi_{11}E_r, \\ D_\theta &= e_{15}\gamma_{\theta z} + \Xi_{11}E_\theta, \\ D_z &= \bar{e}_{31}(\varepsilon_{rr} + \varepsilon_{\theta\theta}) + \bar{\Xi}_{33}E_z, \end{aligned} \tag{6a–c}$$

where $\bar{\Xi}_{33}$ is the reduced dielectric constant, Ξ_{11} and Ξ_{33} are the dielectric constants, all of the piezoelectric layer, and $\bar{\Xi}_{33} = \Xi_{33} + e_{33}^2/C_{33}^E$.

3. Piezoelectric sandwich Kirchhoff plate

In most practical applications of piezoelectric coupled annular plate shown in Fig. 1, the ratio of its radius to the thickness of host plate is more than ten. As such, Kirchhoff assumption for thin plates is applicable, where shear deformation and rotary inertia can be omitted.

3.1. Basic equations

The displacement field in Kirchhoff plate is assumed as follows:

$$\begin{aligned} u_r &= -z\frac{\partial u_z}{\partial r}, \\ u_\theta &= -z\frac{\partial u_z}{r\partial\theta}, \\ u_z &= w(r,\ \theta,\ t), \end{aligned} \tag{7a–c}$$

where $w(r,\ \theta,\ t)$ is the transverse displacement of the mid-plane. The distribution of the electric potential in the thickness direction is assumed to be sinusoidal [7], that is

$$\phi = \varphi(r,\ \theta,\ t)\sin\left(\frac{\pi(z-h)}{h_1}\right), \tag{8}$$

where φ is the electric potential on the mid-surface of the piezoelectric layer, h and h_1 are the thickness of the host plate and the piezoelectric layer, respectively.

The resultant moments and shear forces can be expressed as follows by substituting Eqs. (2)–(8) into Eq. (1):

$$M_{rr} = -\left[(d_1+d_2)\frac{\partial^2 w}{\partial r^2} + (d_1+d_2-2A_1)\left(\frac{\partial w}{r\partial r} + \frac{\partial^2 w}{r^2\partial\theta^2}\right) + \frac{4}{\pi}h_1\bar{e}_{31}\varphi\right],$$

$$M_{\theta\theta} = -\left[(d_1+d_2-2A_1)\frac{\partial^2 w}{\partial r^2} + (d_1+d_2)\left(\frac{\partial w}{r\partial r} + \frac{\partial^2 w}{r^2\partial\theta^2}\right) + \frac{4}{\pi}h_1\bar{e}_{31}\varphi\right],$$

$$M_{r\theta} = -2A_1\left(\frac{\partial^2 w}{r\partial r\partial\theta} - \frac{\partial^2 w}{r^2\partial\theta^2}\right), \tag{9a–c}$$

$$Q_r = -\left[(d_1+d_2)\frac{\partial}{\partial r}\Delta w + \frac{4}{\pi}h_1\bar{e}_{31}\frac{\partial\varphi}{\partial r}\right],$$
$$Q_\theta = -\frac{1}{r}\left[(d_1+d_2)\frac{\partial}{\partial\theta}\Delta w + \frac{4}{\pi}h_1\bar{e}_{31}\frac{\partial\varphi}{\partial\theta}\right], \tag{10a, b}$$

where

$$d_1 = \frac{2}{3}\frac{Eh^3}{1-\mu^2}, \quad d_2 = \tfrac{2}{3}C_{11}^E\left[(h+h_1)^3 - h^3\right] \quad \text{and} \quad A_1 = \frac{1}{2}\left[(1-\mu)d_1 + \left(1 - \frac{C_{12}^E}{C_{11}^E}\right)d_2\right].$$

The governing equation for the Kirchhoff plate is given by

$$\frac{\partial Q_r}{\partial r} + \frac{\partial Q_\theta}{r\partial\theta} + \frac{Q_r}{r} = \int_{-h}^{h}\rho_1\frac{\partial^2 u_z}{\partial t^2}\,\mathrm{d}z + 2\int_{h}^{h+h_1}\rho_2\frac{\partial^2 u_z}{\partial t^2}\,\mathrm{d}z, \tag{11}$$

where ρ_1 and ρ_2 are the material densities of the host material and piezoelectric layer, respectively.

The electrical variables must also satisfy the Maxwell equations which require that the divergence of the electric flux vanishes at any point within the piezoelectric layers. This condition can be satisfied approximately by enforcing the integration of the divergence of the electric flux across the thickness of the piezoelectric layers to vanish for any r and θ:

$$\int_{h}^{h+h_1}\left(\frac{\partial(rD_r)}{r\partial r} + \frac{\partial D_\theta}{r\partial\theta} + \frac{\partial D_z}{\partial z}\right)\mathrm{d}z = 0. \tag{12}$$

The solutions of w and ϕ for wave propagation in θ direction can be written as

$$w(r,\ \theta,\ t) = \bar{w}(r)\mathrm{e}^{\mathrm{i}(p\theta-\omega t)},$$
$$\varphi(r,\ \theta,\ t) = \bar{\varphi}(r)\mathrm{e}^{\mathrm{i}(p\theta-\omega t)}. \tag{13a, b}$$

Substituting Eq. (13) into Eqs. (11) and (12) gives

$$(d_1+d_2)\Delta\Delta\bar{w} + \frac{4}{\pi}h_1\bar{e}_{31}\Delta\bar{\varphi} - A_2\omega^2\bar{w} = 0,$$
$$\tfrac{h_1^2\Xi_{11}}{\pi^2\bar{\Xi}_{33}}\Delta\bar{\varphi} - \bar{\varphi} + \tfrac{h_1^2\bar{e}_{31}}{2\pi^2\bar{\Xi}_{33}} = 0, \tag{14a, b}$$

where

$$\Delta = \frac{\partial^2}{\partial r^2} + \frac{\partial}{r\partial r} - \frac{p^2}{r^2}, \quad A_2 = 2(\rho_1 h + \rho_2 h_1).$$

3.2. Solutions for w and ϕ

Transformation of variable, similar to that in Ref. [1], is adopted. That is,

$$\bar{\varphi} = x\bar{w}, \tag{15}$$

where x is a constant. Substituting Eq. (15) into Eq. (14), gives

$$\Delta\left[\Delta\bar{w} - \frac{A_2\omega^2 h_1^2(2\Xi_{11}x + \bar{e}_{31}\pi) - 8\pi\bar{\Xi}_{33}\bar{e}_{31}h_1x^2}{2\pi^2\bar{\Xi}_{33}(d_1+d_2)}\bar{w}\right] = 0,$$
$$\Delta\bar{w} - \frac{2\pi^2\bar{\Xi}_{33}x}{h_1^2(2\Xi_{11}x + \bar{e}_{31}\pi)}\bar{w} = 0. \tag{16a, b}$$

The solution for $\bar{w}$ is unique under the following conditions:

$$\frac{A_2\omega^2 h_1^2(2\Xi_{11}x + \bar{e}_{31}\pi) - 8\pi\bar{\Xi}_{33}\bar{e}_{31}h_1x^2}{2\pi^2\bar{\Xi}_{33}(d_1+d_2)x} = \frac{2\pi^2\bar{\Xi}_{33}x}{h_1^2(2\Xi_{11}x + \bar{e}_{31}\pi)},$$
$$\frac{2\pi^2\bar{\Xi}_{33}x}{h_1^2(2\Xi_{11}x + \bar{e}_{31}\pi)} = \lambda, \tag{17a, b}$$

where λ is a constant. Under the above condition, Eq. (16) can be reduced to

$$\Delta\bar{w} - \lambda\bar{w} = 0. \tag{18}$$

Eq. (17a) is cubic in x, which gives three roots, $x_i\,(i = 1, 2, 3)$ and $\lambda_i\,(i = 1, 2, 3)$ can be calculated correspondingly from Eq. (17b). Three sets of Bessel functions $c_i w_{i1}(p, \delta_i r) + c_{i+3}w_{i2}(p, \delta_i r)$, $i = 1, 2, 3$ where $\delta_i = \sqrt{|\lambda_i|}$ can be obtained by substituting $\lambda_i\,(i = 1, 2, 3)$ into Eq. (18). The final solutions are given as

$$w = \sum_{i=1}^{3}[c_i w_{i1}(p, \delta_i r) + c_{i+3}w_{i2}(p, \delta_i r)]\mathrm{e}^{\mathrm{i}(p\theta - \omega t)},$$
$$\varphi = \sum_{i=1}^{3} x_i[c_i w_{i1}(p, \delta_i r) + c_{i+3}w_{i2}(p, \delta_i r)]\mathrm{e}^{\mathrm{i}(p\theta - \omega t)}, \tag{19a, b}$$

where

$$w_{i1}(p, \delta_i r) = \begin{cases} J_p(\delta_i r) & \lambda_i < 0, \\ I_p(\delta_i r) & \lambda_i > 0, \end{cases} \quad i = 1, 2, 3,$$
$$w_{i2}(p, \delta_i r) = \begin{cases} Y_p(\delta_i r) & \lambda_i < 0, \\ K_p(\delta_i r) & \lambda_i > 0, \end{cases} \tag{20a–d}$$

where J and Y are Bessel functions of the first and second kind, respectively, I and K are modified Bessel functions of the first and second kind, respectively, and $c_i\,(i = 1, \ldots, 6)$ are six constants of integration.

As usual, the determinant of the matrix containing the system frequencies is considered after imposing the electric and displacement boundary conditions. If the plate is insulated at the edge, the electrical flux conservation equation is given by

$$\int_h^{h+h_1} D_r(r, \theta, t)\,\mathrm{d}z = 0. \tag{21}$$

Substituting Eq. (6a) into Eq. (21) in view of $\gamma_{rz} = 0$, yields the electric boundary condition

$$\frac{\partial \varphi}{\partial r} = 0. \tag{22}$$

The standard boundary conditions for the clamped, simply supported and free ends are given respectively as follows:

(i) *Clamped*:

$$\begin{aligned} w(r_1, \theta, t) &= \frac{\partial w}{\partial r}_{r=r_1} = \frac{\partial \varphi}{\partial r}_{r=r_1} = 0, \\ w(r_0, \theta, t) &= \frac{\partial w}{\partial r}_{r=r_0} = \frac{\partial \varphi}{\partial r}_{r=r_0} = 0. \end{aligned} \tag{23a, b}$$

(ii) *Simply supported*:

$$\begin{aligned} w(r_1, \theta, t) = M_{rr}(r_1, \theta, t) &= \frac{\partial \varphi}{\partial r}_{r=r_1} = 0, \\ w(r_0, \theta, t) = M_{rr}(r_0, \theta, t) &= \frac{\partial \varphi}{\partial r}_{r=r_0} = 0. \end{aligned} \tag{24a, b}$$

(iii) *Free*:

$$\begin{aligned} M_{rr}(r_1, \theta, t) = Q(r_1, \theta, t) &= \frac{\partial \varphi}{\partial r}_{r=r_1} = 0, \\ M_{rr}(r_0, \theta, t) = Q(r_0, \theta, t) &= \frac{\partial \varphi}{\partial r}_{r=r_0} = 0. \end{aligned} \tag{25a, b}$$

For all possible combinations of clamped, simply supported and free edge conditions at the inner ($r = r_1$) and outer ($r = r_0$) circular boundaries of the annular plate (Fig. 1), a matrix involving the system frequencies can always be formulated. For example, the determinant of frequencies under clamped–clamped (C–C) boundary condition is given by substituting Eq. (19)

into Eq. (23), resulting in

$$\begin{vmatrix} w_{11}(p,\delta_1 r_1) & w_{12}(p,\delta_1 r_1) & w_{21}(p,\delta_2 r_1) & w_{22}(p,\delta_2 r_1) & w_{31}(p,\delta_3 r_1) & w_{32}(p,\delta_3 r_1) \\ w'_{11}(p,\delta_1 r_1) & w'_{12}(p,\delta_1 r_1) & w'_{21}(p,\delta_2 r_1) & w'_{22}(p,\delta_2 r_1) & w'_{31}(p,\delta_3 r_1) & w'_{32}(p,\delta_3 r_1) \\ x_1 w'_{11}(p,\delta_1 r_1) & x_1 w'_{12}(p,\delta_1 r_1) & x_2 w'_{21}(p,\delta_2 r_1) & x_2 w'_{22}(p,\delta_2 r_1) & x_3 w'_{31}(p,\delta_3 r_1) & x_3 w'_{32}(p,\delta_3 r_1) \\ w_{11}(p,\delta_1 r_0) & w_{12}(p,\delta_1 r_0) & w_{21}(p,\delta_2 r_0) & w_{22}(p,\delta_2 r_0) & w_{31}(p,\delta_3 r_0) & w_{32}(p,\delta_3 r_0) \\ w'_{11}(p,\delta_1 r_0) & w'_{12}(p,\delta_1 r_0) & w'_{21}(p,\delta_2 r_0) & w'_{22}(p,\delta_2 r_0) & w'_{31}(p,\delta_3 r_0) & w'_{32}(p,\delta_3 r_0) \\ x_1 w'_{11}(p,\delta_1 r_0) & x_1 w'_{12}(p,\delta_1 r_0) & x_2 w'_{21}(p,\delta_2 r_0) & x_2 w'_{22}(p,\delta_2 r_0) & x_3 w'_{31}(p,\delta_3 r_0) & x_3 w'_{32}(p,\delta_3 r_0) \end{vmatrix}, \tag{26}$$

where the prime $'$ denotes $\partial/\partial r$, and w_{ij} is given in Eq. (20). Setting Eq. (26) to zero yields the resonant frequencies and their corresponding mode shapes.

4. Piezoelectric sandwich mindlin plate

In some applications of piezoelectric sandwich plate, the number of nodal diameters (i.e. number of zeros in the θ-direction) is relatively large and the wavelength is not necessarily small compared to the plate thickness. This suggests that shear deformations and/or rotary inertia have to be taken into account.

4.1. Basic equations

Mindlin [15] and Mindlin and Medick [16] corrected for the effect of shear and rotary inertia in the plate model and obtained results of wave propagation agreeing better with those using the exact theory. The modified expression for displacement field is written as

$$\begin{aligned} u_r &= z\psi_r(r,\theta,t), \\ u_\theta &= z\psi_\theta(r,\theta,t), \\ u_z &= w(r,\theta,t), \end{aligned} \tag{27a–c}$$

where ψ_r and ψ_θ are the rotations of the normal to the mid-plane, measured on the z–r and z–θ planes, respectively.

Substituting Eqs. (2)–(6), (8) and (27) into Eq. (1) yields the following resultant moments and shear forces:

$$M_{rr} = (d_1+d_2)\frac{\partial\psi_r}{\partial r} + (d_1+d_2-2A_1)\left(\frac{\psi_r}{r}+\frac{\partial\psi_\theta}{r\partial\theta}\right) - \frac{4}{\pi}h_1\bar{e}_{31}\varphi,$$

$$M_{\theta\theta} = (d_1+d_2-2A_1)\frac{\partial\psi_r}{\partial r} + (d_1+d_2)\left(\frac{\psi_r}{r}+\frac{\partial\psi_\theta}{r\partial\theta}\right) - \frac{4}{\pi}h_1\bar{e}_{31}\varphi,$$

$$M_{r\theta} = A_1\left(\frac{\partial \psi_r}{r\partial\theta} - \frac{\psi_\theta}{r} + \frac{\partial \psi_\theta}{\partial r}\right), \tag{28a–c}$$

$$Q_r = A_3\left(\frac{\partial w}{\partial r} + \psi_r\right) - \frac{4}{\pi}h_1 e_{15}\frac{\partial \varphi}{\partial r},$$

$$Q_\theta = A_3\left(\frac{\partial w}{r\partial\theta} + \psi_\theta\right) - \frac{4}{\pi}h_1 e_{15}\frac{\partial \varphi}{r\partial\theta}, \tag{29a, b}$$

where $A_3 = \kappa^2\left(Eh/(1+\mu) + 2h_1 C_{55}^E\right)$.

It is to be noted that M_{rr}, $M_{r\theta}$, $M_{\theta\theta}$, Q_r and Q_θ must satisfy Maxwell equation (12) and the following dynamic equilibrium equations:

$$\frac{\partial Q_r}{\partial r} + \frac{\partial Q_\theta}{r\partial\theta} + \frac{Q_r}{r} = \int_{-h}^{h}\rho_1\frac{\partial^2 u_z}{\partial t^2}\,\mathrm{d}z + 2\int_{h}^{h+h_1}\rho_2\frac{\partial^2 u_z}{\partial t^2}\,\mathrm{d}z,$$

$$\frac{\partial M_{rr}}{\partial r} + \frac{\partial M_{r\theta}}{r\partial\theta} + \frac{M_{rr} - M_{r\theta}}{r} - Q_r = \int_{-h}^{h}\rho_1 z\frac{\partial^2 u_r}{\partial t^2}\,\mathrm{d}z + 2\int_{h}^{h+h_1}\rho_2 z\frac{\partial^2 u_r}{\partial t^2}\,\mathrm{d}z,$$

$$\frac{\partial M_{r\theta}}{\partial r} + \frac{\partial M_{\theta\theta}}{r\partial\theta} + \frac{2M_{r\theta}}{r} - Q_\theta = \int_{-h}^{h}\rho_1 z\frac{\partial^2 u_\theta}{\partial t^2}\,\mathrm{d}z + 2\int_{h}^{h+h_1}\rho_2 z\frac{\partial^2 u_\theta}{\partial t^2}\,\mathrm{d}z. \tag{30a–c}$$

The rotations ψ_r and ψ_θ are expressed through the transformation [15]

$$\psi_r = \frac{\partial R}{\partial r} + \frac{\partial H}{r\partial\theta},$$

$$\psi_\theta = \frac{\partial R}{r\partial\theta} - \frac{\partial H}{\partial r}. \tag{31a, b}$$

It is assumed that the solutions of w, R, H and ϕ for wave propagation in the θ direction take the form

$$w(r,\theta,t) = \bar{w}(r)\cos(p\theta)\mathrm{e}^{\mathrm{i}\omega t},$$

$$R(r,\theta,t) = \bar{R}(r)\cos(p\theta)\mathrm{e}^{\mathrm{i}\omega t},$$

$$H(r,\theta,t) = \bar{H}(r)\sin(p\theta)\mathrm{e}^{\mathrm{i}\omega t},$$

$$\varphi(r,\theta,t) = \bar{\varphi}(r)\cos(p\theta)\mathrm{e}^{\mathrm{i}\omega t}. \tag{32a–d}$$

Eq. (32a–d) is adopted as it represents harmonic oscillation and is consistent with the assumption that the plate undergoes small synchronous free vibratory motions. To satisfy Eq. (30a–c), the sine instead of cosine function is employed for $H(r,\ \theta,\ t)$.

Substituting Eqs. (31) and (32) into Eqs. (12) and (30) gives

$$A_3\Delta\bar{R} + A_3\Delta\bar{w} + A_2\omega^2\bar{w} - A_6\Delta\bar{\varphi} = 0,$$

$$\frac{\partial}{\partial r}[(d_1+d_2)\Delta\bar{R} - (A_3 - A_4\omega^2)\bar{R} - A_3\bar{w} + A_5\bar{\varphi}] + \frac{p}{r}[A_1\Delta\bar{H} - (A_3 - A_4\omega^2)\bar{H}] = 0,$$

$$\frac{p}{r}[(d_1+d_2)\Delta\bar{R} - (A_3 - A_4\omega^2)\bar{R} - A_3\bar{w} + A_5\bar{\varphi}] + \frac{\partial}{\partial r}[A_1\Delta\bar{H} - (A_3 - A_4\omega^2)\bar{H}] = 0,$$

$$\Delta\bar{R} + A_7\Delta\bar{w} - A_8\Delta\bar{\varphi} - A_9\bar{\varphi} = 0, \tag{33a–d}$$

where

$$\Delta = \frac{\partial^2}{\partial r^2} + \frac{\partial}{r\partial r} - \frac{p^2}{r^2}, \quad A_4 = \tfrac{2}{3}[(\rho_1 - \rho_2)h^3 + \rho_2(h + h_1)^3], \quad A_5 = \frac{4h_1}{\pi}(e_{15} - \bar{e}_{31}),$$
$$A_6 = \frac{4h_1 e_{15}}{\pi}, \quad A_7 = \frac{e_{15}}{e_{15} + \bar{e}_{31}}, \quad A_8 = \frac{2\Xi_{11}}{(e_{15} + \bar{e}_{31})\pi}, \quad A_9 = \frac{2\Xi_{11}\pi}{(e_{15} + \bar{e}_{31})h_1^2}.$$

4.2. Solutions for w, ψ_r ψ_θ and ϕ

$\bar{H}$ can be separated from $\bar{R}$ and $\bar{w}$ by differentiation, addition, and subtraction of Eqs. (33b) and (33c). These two equations become

$$\Delta[A_1\Delta\bar{H} - (A_3 - A_4\omega^2)\bar{H}] = 0,$$
$$\Delta[(d_1 + d_2)\Delta\bar{R} - (A_3 - A_4\omega^2)\bar{R} - A_3\bar{w} + A_5\bar{\varphi}] = 0. \tag{34a, b}$$

To uncouple $\bar{R}$, $\bar{\varphi}$ and $\bar{w}$ in Eqs. (33a), (33d), and (34b), transformation of variables is applied, similar to that in [1,15]

$$\bar{R} = x\bar{w},$$
$$\bar{\varphi} = y\bar{w}, \tag{35a, b}$$

where x, y are constants. Eqs. (33a), (33d), and (34b) can then be simplified to

$$\Delta\left[\Delta\bar{w} - \frac{A_3 - A_5 y + (A_3 - A_4\omega^2)x}{(d_1 + d_2)x}\bar{w}\right] = 0,$$
$$\Delta\bar{w} - \frac{A_2\omega^2}{A_6 y - A_3(x + 1)}\bar{w} = 0,$$
$$\Delta\bar{w} - \frac{A_9 y}{A_8 y - x - A_7}\bar{w} = 0, \tag{36a–c}$$

respectively. Observe that the terms within the brackets in Eqs. (36a), (36b) and (36c) are of identical form. Hence, for the solution of $\bar{w}$ to be unique,

$$\frac{(A_3 - A_4\omega^2)x + A_3 - A_5 y}{(d_1 + d_2)x} = \frac{A_2\omega^2}{A_6 y - A_3(x + 1)} = \frac{A_9 y}{A_8 y - x - A_7},$$
$$\frac{A_9 y}{A_8 y - x - A_7} = \lambda. \tag{37a, b}$$

Eq. (36) can be thus reduced to

$$\Delta\bar{w} - \lambda\bar{w} = 0, \tag{38}$$

where λ is a constant. Eq. (37a) is cubic in x and y, which give three pairs of roots, $x_i, y_i\,(i = 1, 2, 3)$, from which $\lambda_i\,(i = 1, 2, 3)$ can be computed using Eq. (37b). Three sets of Bessel functions $c_i w_{i1}(p, \delta_i r) + c_{i+3} w_{i2}(p, \delta_i r), i = 1, 2, 3$ where $\delta_i = \sqrt{|\lambda_i|}$ are obtained by substituting

$\lambda_i\,(i=1,\ 2,\ 3)$ into Eq. (38a). The final solutions are given as

$$w=\sum_{i=1}^{3}[c_i w_{i1}(p,\delta_i r)+c_{i+3}w_{i2}(p,\delta_i r)]\cos(p\theta)\mathrm{e}^{\mathrm{i}\omega t},$$

$$R=\sum_{i=1}^{3}x_i[c_i w_{i1}(p,\delta_i r)+c_{i+3}w_{i2}(p,\delta_i r)]\cos(p\theta)\mathrm{e}^{\mathrm{i}\omega t},$$

$$\varphi=\sum_{i=1}^{3}y_i[c_i w_{i1}(p,\delta_i r)+c_{i+3}w_{i2}(p,\delta_i r)]\cos(p\theta)\mathrm{e}^{\mathrm{i}\omega t}, \tag{39a–c}$$

where the definition of $w_{i1}(p,\delta_i r)$ and $w_{i2}(p,\delta_i r)$ are the same as Eq. (20); and $c_i\,(i=1,\ldots,6)$ are integration constants.

Substituting Eq. (36a) into Eqs. (33b) and (33c), gives the following Bessel equation:

$$\Delta\bar{H}-\lambda_4\bar{H}=0, \tag{40a, b}$$

where

$$\lambda_4=\frac{A_3-A_4\omega^2}{A_1}.$$

Finally, H can be expressed as

$$H=[c_7 w_{41}(p,\delta_4 r)+c_8 w_{42}(p,\delta_4 r)]\sin(p\theta)\mathrm{e}^{\mathrm{i}\omega t}, \tag{41}$$

where $\delta_4=\sqrt{|\lambda_4|}$ and the definition of $w_{41}(p,\delta_4 r)$ and $w_{42}(p,\delta_4 r)$ is the same as Eq. (20); and $c_i\,(i=7,\ 8)$ are integration constants.

Substituting Eqs. (39b) and (41) into Eq. (31) gives

$$\psi_r=\left[\sum_{i=1}^{3}x_i\left(c_i\frac{\partial w_{i1}}{\partial r}+c_{i+3}\frac{\partial w_{i2}}{\partial r}\right)+\frac{p}{r}(c_7 w_{41}+c_8 w_{42})\right]\cos(p\theta)\mathrm{e}^{\mathrm{i}\omega t},$$

$$\psi_\theta=-\left[\frac{p}{r}\sum_{i=1}^{3}x_i(c_i w_{i1}+c_{i+3}w_{i2})+\left(c_7\frac{\partial w_{41}}{\partial r}+c_8\frac{\partial w_{42}}{\partial r}\right)\right]\sin(p\theta)\mathrm{e}^{\mathrm{i}\omega t}. \tag{42a, b}$$

The determinant of the matrix of system frequencies is generated after imposing the electric and displacement boundary conditions. The electric boundary condition can be obtained by substituting Eq. (6a) into Eq. (21) giving

$$e_{15}\pi\left(\psi_r+\frac{\partial w}{\partial r}\right)-2\Xi_{11}\frac{\partial\varphi}{\partial r}=0. \tag{43}$$

The standard boundary conditions for the clamped, simply supported (soft type) and free ends are given respectively as follows:

(i) *Clamped:*

$$w(r_1,\theta,t)=\psi_r(r_1,\theta,t)=\psi_\theta(r_1,\theta,t)=[e_{15}\pi(\psi_r+\frac{\partial w}{\partial r})-2\Xi_{11}\frac{\partial\varphi}{\partial r}]_{r=r_1}=0,$$
$$w(r_0,\theta,t)=\psi_r(r_0,\theta,t)=\psi_\theta(r_0,\theta,t)=[e_{15}\pi(\psi_r+\frac{\partial w}{\partial r})-2\Xi_{11}\frac{\partial\varphi}{\partial r}]_{r=r_0}=0. \quad (44a, b)$$

(ii) *Simply supported (soft type):*

$$w(r_1,\theta,t)=M_{rr}(r_1,\theta,t)=M_{r\theta}(r_1,\theta,t)=[e_{15}\pi(\psi_r+\frac{\partial w}{\partial r})-2\Xi_{11}\frac{\partial\varphi}{\partial r}]_{r=r_1}=0,$$
$$w(r_0,\theta,t)=M_{rr}(r_0,\theta,t)=M_{r\theta}(r_0,\theta,t)=[e_{15}\pi(\psi_r+\frac{\partial w}{\partial r})-2\Xi_{11}\frac{\partial\varphi}{\partial r}]_{r=r_0}=0. \quad (45a, b)$$

(iii) *Free:*

$$M_{rr}(r_1,\theta,t)=M_{r\theta}(r_1,\theta,t)=Q_r(r_1,\theta,t)=[e_{15}\pi(\psi_r+\frac{\partial w}{\partial r})-2\Xi_{11}\frac{\partial\varphi}{\partial r}]_{r=r_1}=0,$$
$$M_{rr}(r_0,\theta,t)=M_{r\theta}(r_0,\theta,t)=Q_r(r_0,\theta,t)=[e_{15}\pi(\psi_r+\frac{\partial w}{\partial r})-2\Xi_{11}\frac{\partial\varphi}{\partial r}]_{r=r_0}=0. \quad (46a, b)$$

For all possible combinations of clamped, simply supported and free edge conditions at the inner ($r=r_1$) and outer ($r=r_0$) circular boundaries of the annular plate (Fig. 1), a matrix of system frequencies can be formulated. For example, the determinant of system frequencies under clamped–clamped (C–C) boundary condition is given by substituting Eqs. (39a), (39c), and (42) into Eq. (44):

$$\begin{vmatrix}
w_{11}(\delta_1 r_1) & w_{12}(\delta_1 r_1) & w_{21}(\delta_2 r_1) & w_{22}(\delta_2 r_1) & w_{31}(\delta_3 r_1) & w_{32}(\delta_3 r_1) & 0 & 0\\
x_1 w'_{11}(\delta_1 r_1) & x_1 w'_{12}(\delta_1 r_1) & x_2 w'_{21}(\delta_2 r_1) & x_2 w'_{22}(\delta_2 r_1) & x_3 w'_{31}(\delta_3 r_1) & x_3 w'_{32}(\delta_3 r_1) & \frac{p}{r_1} w_{41}(\delta_4 r_1) & \frac{p}{r_1} w_{42}(\delta_4 r_1)\\
\frac{px_1}{r_1} w_{11}(\delta_1 r_1) & \frac{px_1}{r_1} w_{12}(\delta_1 r_1) & \frac{px_2}{r_1} w_{21}(\delta_2 r_1) & \frac{px_2}{r_1} w_{22}(\delta_2 r_1) & \frac{px_3}{r_1} w_{31}(\delta_3 r_1) & \frac{px_3}{r_1} w_{32}(\delta_3 r_1) & w'_{41}(\delta_4 r_1) & w'_{42}(\delta_4 r_1)\\
\varphi_{11}(r_1) & \varphi_{12}(r_1) & \varphi_{21}(r_1) & \varphi_{22}(r_1) & \varphi_{31}(r_1) & \varphi_{32}(r_1) & 0 & 0\\
w_{11}(\delta_1 r_0) & w_{12}(\delta_1 r_0) & w_{21}(\delta_2 r_0) & w_{22}(\delta_2 r_0) & w_{31}(\delta_3 r_0) & w_{32}(\delta_3 r_0) & 0 & 0\\
x_1 w'_{11}(\delta_1 r_0) & x_1 w'_{12}(\delta_1 r_0) & x_2 w'_{21}(\delta_2 r_0) & x_2 w'_{22}(\delta_2 r_0) & x_3 w'_{31}(\delta_3 r_0) & x_3 w'_{32}(\delta_3 r_0) & \frac{p}{r_0} w_{41}(\delta_4 r_0) & \frac{p}{r_0} w_{42}(\delta_4 r_0)\\
\frac{px_1}{r_0} w_{11}(\delta_1 r_0) & \frac{px_1}{r_0} w_{12}(\delta_1 r_0) & \frac{px_2}{r_0} w_{21}(\delta_2 r_0) & \frac{px_2}{r_0} w_{22}(\delta_2 r_0) & \frac{px_3}{r_0} w_{31}(\delta_3 r_0) & \frac{px_3}{r_0} w_{32}(\delta_3 r_0) & w'_{41}(\delta_4 r_0) & w'_{42}(\delta_4 r_0)\\
\varphi_{11}(r_0) & \varphi_{12}(r_0) & \varphi_{21}(r_0) & \varphi_{22}(r_0) & \varphi_{31}(r_0) & \varphi_{32}(r_0) & 0 & 0
\end{vmatrix}, \quad (47)$$

where $w_{ij}(p,\delta_i r)$ is expressed as $w_{ij}(\delta_i r)$ for concise notation, the factors $\cos(p\theta)e^{i\omega t}$ and $\sin(p\theta)e^{i\omega t}$ have been omitted; $(\,)'=\partial/\partial r$, and

$$\varphi_{ij}(r_0)=e_{15}\pi x_i w_{ij}(p,\delta_i r_0)+(e_{15}\pi-2\Xi_{11}y_i)w'_{ij}(p,\delta_i r_0),$$
$$\varphi_{ij}(r_1)=e_{15}\pi x_i w_{ij}(p,\delta_i r_1)+(e_{15}\pi-2\Xi_{11}y_i)w'_{ij}(p,\delta_i r_1),\quad i=1,2,3,\quad j=1,2.$$

Setting Eq. (47) to zero yields the resonant frequencies and their corresponding mode shapes.

5. Numerical examples and discussion

The numerical solution for a three-layer laminated annular plate shown in Fig. 1 is investigated. The material for the host plate is steel and that of the piezoelectric layer is PZT4. Their properties are listed in Table 1. The inner radius (r_1) and outer radius (r_0) of the annular plate are 0.1 m and 0.6 m, respectively.

5.1. Comparison between proposed models and FEM

To investigate the difference between CPT- and IPT-based model, two steel plates with thickness, $h = 0.01$ m and 0.03 m, are studied under four kinds of boundary conditions: C–C, S–C, C–S and S–S, where the first and second letter denotes the edge condition at the inner and outer edge, respectively, C denotes clamped and S denotes simply supported. The thickness ratio of the piezoelectric layer to the host plate is 1/10. The results are compared with those from 3D FE analyses using ABAQUS 6.3.

Table 2 lists the frequencies for the free vibration of the annular plate with $h = 0.01$ m corresponding to thin plate, for mode shapes with 0 to 2 diametrical nodes (denoted by p) and 0 to 2 nodal circles (denoted by n). For a thin plate with large radius–thickness ratio ($r_0/h = 20$), the frequencies from both CPT- and IPT-based model are in close agreement with the FE results. The IPT-based model produces (slightly lower) results almost coincident with those from FE analysis while the results from CPT-based model produces higher results but differ by less than 5% for all modes listed in Table 2.

Table 3 lists the frequencies for the free vibration of the annular plate with $h = 0.03$ m corresponding to moderately thick plate, for mode shapes with 0 to 2 diametrical nodes and 0 to 2 nodal circles. As the radius–thickness ratio is small ($r_0/h = 20$), the IPT-based model provides results lower than those from FE analysis, with a maximum difference of only 3.4% for the case

Table 1
Material properties

Property	Host structure (steel)	Piezoelectric layer (PZT4)
Young's modulus (N/m^2)	$E = 200 \times 10^9$	$C_{11}^E = 132 \times 10^9$ $C_{12}^E = 71 \times 10^9$ $C_{33}^E = 115 \times 10^9$ $C_{13}^E = 73 \times 10^9$ $C_{55}^E = 73 \times 10^9$
Poisson ratio	0.3	—
Mass density (kg/m^3)	7.8×10^3	7.5×10^3
e_{31} (C/m^2)	—	−4.1
e_{33} (C/m^2)	—	14.1
e_{15} (C/m^2)	—	10.5
Ξ_{11} (F/m)	—	7.124×10^{-9}
Ξ_{33} (F/m)	—	5.841×10^{-9}

Table 2
Comparison of frequencies (rad/s) of thin annular plate under C–C, C–S, S–C, S–S boundary conditions for $r_0/h = 60$

BC	p	n	FEM	CPT-based model	Error (%)	IPT-based model	Error (%)
C[a]–C	0	0	2812	2815	0.09	2769	−1.53
		1	7659	7786	1.66	7517	−1.85
		2	14,753	15,306	3.75	14,428	−2.20
	1	0	2942	2952	0.36	2899	−1.43
		1	7882	8030	1.87	7743	−1.76
		2	15,020	15,608	3.91	14,698	−2.14
	2	0	3471	3506	0.99	3438	−0.97
		1	8635	8840	2.38	8507	−1.48
		2	15,877	16,569	4.36	15,566	−1.96
C–S	0	0	1848	1843	−0.31	1823	−1.36
		1	6164	6220	0.92	6066	−1.59
		2	12,770	13,111	2.67	12,523	−1.94
	1	0	1981	1983	0.10	1957	−1.21
		1	6384	6459	1.16	6289	−1.50
		2	13,038	13,411	2.86	12,794	−1.87
	2	0	2511	2535	0.95	2495	−0.62
		1	7134	7259	1.75	7050	−1.17
		2	13,903	14,367	3.34	13,672	−1.66
S–C	0	0	2213	2216	0.12	2194	−0.86
		1	6544	6615	1.08	6455	−1.37
		2	13,169	13,531	2.75	12,934	−1.78
	1	0	2418	2446	1.13	2397	−0.89
		1	6865	6983	1.72	6774	−1.32
		2	13,528	13,961	3.20	13,293	−1.74
	2	0	3178	3236	1.81	3159	−0.61
		1	7902	8119	2.74	7815	−1.11
		2	14,663	15,274	4.16	14,428	−1.61
S–S	0	0	1395	1396	0.04	1388	−0.51
		1	5173	5198	0.49	5115	−1.11
		2	11,283	11,489	1.82	11,114	−1.50
	1	0	1593	1613	1.30	1583	−0.58
		1	5490	5558	1.23	5433	−1.05
		2	11,647	11,918	2.32	11,478	−1.45
	2	0	2312	2355	1.84	2306	−0.25
		1	6521	6669	2.27	6468	−0.82
		2	12,798	13,225	3.34	12,632	−1.30

p = Number of nodal diameters, n = number of nodal circles, C = clamped, S = simply supported.
[a]First letter denotes edge condition at inner edge.

where $p = 2$, $n = 2$ under C–C boundary condition while the frequencies computed by CPT-based model can be 39.7% greater than those by FE analysis.

Both the CPT- and IPT-based model give results closer to the FE analysis results at lower frequencies than they do at higher frequencies as shown in Tables 2 and 3. For example, in

Table 3
Comparison of frequencies (rad/s) of moderately thick annular plate under C–C, C–S, S–C, S–S boundary conditions for $r_0/h = 20$

BC	p	n	FEM	CPT-based model	Error (%)	IPT-based model	Error (%)
C[a]–C	0	0	7608	8444	10.98	7416	−2.52
		1	18,828	23,358	24.06	18,235	−3.15
		2	33,096	45,917	38.74	31,869	−3.71
	1	0	7918	8857	11.86	7728	−2.40
		1	19,358	24,089	24.44	18,774	−3.02
		2	33,685	46,824	39.00	32,468	−3.61
	2	0	9336	10,517	12.65	9169	−1.79
		1	21,199	26,520	25.10	20,639	−2.64
		2	35,591	49,706	39.66	34,397	−3.35
C–S	0	0	5171	5528	6.90	5064	−2.07
		1	15,924	18,661	17.19	15,500	−2.66
		2	30,188	39,332	30.29	29,201	−3.27
	1	0	5512	5950	7.95	5406	−1.91
		1	16,464	19,376	17.69	16,048	−2.52
		2	30,803	40,232	30.61	29,827	−3.17
	2	0	6990	7604	8.79	6907	−1.17
		1	18,376	21,776	18.50	17,986	−2.12
		2	32,806	43,101	31.38	31,854	−2.90
S–C	0	0	6218	6647	6.91	6125	−1.49
		1	16,939	19,845	17.16	16,536	−2.38
		2	31,161	40,594	30.27	30,197	−3.09
	1	0	6664	7337	10.10	6555	−1.64
		1	17,593	20,949	19.07	17,172	−2.39
		2	31,809	41,883	31.67	30,826	−3.09
	2	0	8650	9707	12.22	8528	−1.41
		1	19,909	24,357	22.34	19,453	−2.29
		2	33,990	45,821	34.81	32,959	−3.03
S–S	0	0	4032	4187	3.86	3997	−0.85
		1	14,030	15,593	11.14	13,775	−1.82
		2	28,159	34,466	22.40	27,430	−2.59
	1	0	4498	4840	7.60	4450	−1.06
		1	14,716	16,674	13.30	14,443	−1.86
		2	28,852	35,753	23.92	28,102	−2.60
	2	0	6484	7064	8.94	6433	−0.79
		1	17,162	20,008	16.58	16,859	−1.77
		2	31,183	39,676	27.23	30,385	−2.56

p = Number of nodal diameters, n = number of nodal circles, C = clamped, S = simply supported.
[a]First letter denotes edge condition at inner edge.

Table 3, the CPT-based model gives a frequency 39.7% greater than that of the FE analysis for $p = 2$ and $n = 2$ while it gives a value of only 11.0% greater than that of the FE analysis for $p = 0$ and $n = 0$ under C–C boundary condition. Moreover S–S boundary conditions yield smaller

h(m)	BC	cases	*p*=0, *n*=0	*p*=1, *n*=0	*p*=2, *n*=0
0.01	C-C[a]	FE results	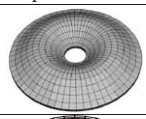	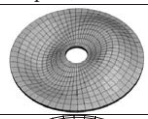	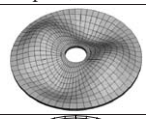
		CPT-based model results	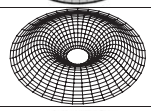	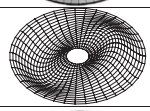	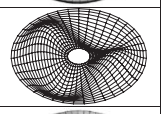
	S-S	FE results	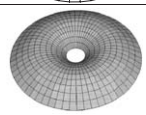	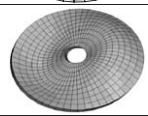	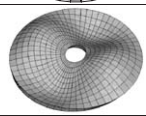
		CPT-based model results	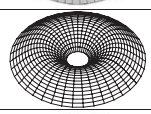	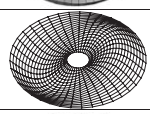	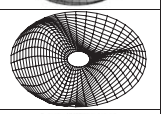
0.03	C-C	FE results	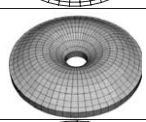	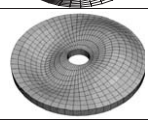	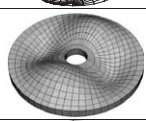
		IPT-based model results	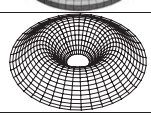	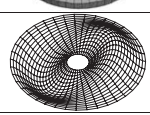	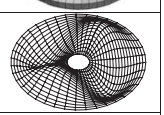
	S-S	FE results	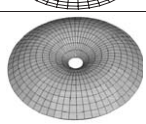	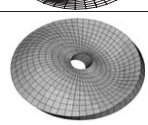	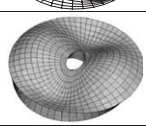
		IPT-based model results	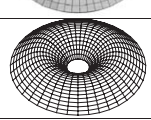	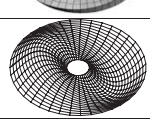	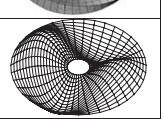

p = number of nodal diameters. *n*= number of nodal circles.
C = clamped, S = simply supported.
[a] first letter denotes edge condition at inner edge.

Fig. 2. Comparison of first three displacement mode shapes for annular plate ($h = 0.01$ for thin plate condition and 0.03 for moderately thick plate condition) under C–C and S–S conditions from FE and proposed solutions.

frequencies than those under C–C, C–S and S–C boundary conditions and hence their results are closer to the FE results. The CPT-based model gives higher frequencies than IPT-based model because the CPT-based model neglects the effect of transverse shear deformation and rotary inertia which implies a stiffer model. Fig. 2 shows the first three mode shapes of the annular plate of thickness $h = 0.01$ m (simulating a thin plate) and 0.03 m (simulating a moderately thick plate) obtained by the proposed model and 3D FE results. The mode shapes for the number of nodal diameters $p = 0$, 1, 2 and number of nodal circles $n = 0$ from the proposed modals and 3D FE are almost identical.

5.2. Effect of piezoelectric layer

To investigate the effect of piezoelectric layer on the vibration of piezoelectric coupled plate, the two plates in Section 5.1 are studied based on the proposed models and FE analysis under C–C boundary condition. Three different thickness ratios of piezoelectric layer to host plate, $h_1/2h = \frac{1}{12}$, $\frac{1}{8}$, and $\frac{1}{5}$, are adopted.

Table 4 lists the frequencies for free vibration modes with $p = 0$–2 diametrical nodes and $n = 0$–2 nodal circles, where the case of $h_1 = 0$ provides the base for comparing the effect of the piezoelectric layer on the frequencies (and stiffness) of the system. For CPT-based model with $r_0/h = 60$ (thin plate), the percentage increase is around 2.7% for all modes with $h_1/2h = 1/12$. The effect is higher for thicker piezoelectric layer where with $h_1/2h = 1/8$, and 1/5, the increase is about 4.9% and 10.0%, respectively, for all modes. This is mainly due to the increase in bending stiffness rather than the piezoelectric effect, as confirmed by results shown in Fig. 3, where the frequency ratio based on FEM simulation under C–C conditions is plotted (full line shows the effect of stiffness due to increase in thickness from piezoelectric layer whereas dotted line shows the effect of piezoelectricity only for this particular PZT4). Similar findings are obtained for $r_0/h = 20$. For IPT-based model when $r_0/h = 60$, first the frequencies are lower than the corresponding CPT-based values even with the presence of piezoelectric layers. Second, the increase in frequency for the IPT-based for $h_1/2h = 1/12$, 1/8, and 1/5 are 2.5%, 4.6% and 9.3% respectively when $p = 0$ and $n = 0$. Both can be attributed by the IPT-model being less stiff. The increase in resonant frequency is smaller for higher modes indicating reduced bending stiffness effect as confirmed by Fig. 3. For example, when $r_0/h = 60$ and $h_1/2h = 1/12$, the increase is 2.5% for $p = 0$ and $n = 0$, and 1.9% for $p = 2$ and $n = 2$. The increase in resonant frequency is also smaller for lower r_0/h values, for example when $r_0/h = 20$ and $h_1/2h = 1/12$, the increase is 1.2% (compared to 2.5% for $r_0/h = 60$ and $h_1/2h = 1/12$) for $p = 0$ and $n = 0$. This effect is not obvious for the CPT-based results as it does not account for the shear effect.

6. Conclusions

The free vibration of a three-layer piezoelectric laminated annular plate based on the Kirchhoff and Mindlin plate theories are investigated for the case where the electrodes on the piezoelectric layers are shortly connected. The electric potential distribution across thickness of piezoelectric layer is modeled by a sinusoidal function and Maxwell equation is enforced. Analytical solutions based on transformation of variables are presented. Numerical validation of the solutions against 3D FE results was performed for annular plates with different radius–thickness ratio under different boundary conditions. The IPT-based model provides results similar to those from FE analysis for both thin and thick plates. The solutions based on CPT-based model are shown to be valid only for thin plates and diverge from the FE results for thick plates, particularly for high frequencies. Results indicate that thicker piezoelectric layer increases the resonant frequencies of the system but the effect is less significant for higher modes and also plates with lower radius to thickness ratio. The analytical solutions provided and the findings will be used in the design of piezoelectric materials in mechanical systems for practical applications, such as the ultrasonic motor.

Table 4
Frequencies (rad/s) of annular plate under C–C boundary condition with piezoelectric layers of different thickness

P	n	$h_1 = 0$	$h_1/2h = 1/12$	Increments(%)	$h_1/2h = 1/8$	Increments(%)	$h_1/2h = 1/5$	Increments(%)
CPT-based model ($r_0/h = 60$)								
0	0	2718	2792	2.70	2853	4.93	2989	9.95
	1	7520	7723	2.70	7891	4.93	8268	9.95
	2	14,783	15,182	2.70	15,512	4.93	16,253	9.95
1	0	2851	2928	2.70	2992	4.93	3135	9.95
	1	7755	7965	2.70	8138	4.93	8527	9.95
	2	15,075	15,482	2.70	15,818	4.93	16,574	9.95
2	0	3385	3477	2.70	3553	4.93	3723	9.95
	1	8538	8768	2.70	8959	4.93	9387	9.95
	2	16,002	16,434	2.70	16,791	4.93	17,594	9.95
CPT-based model ($r_0/h = 20$)								
0	0	8155	8376	2.71	8558	4.93	8967	9.95
	1	22,560	23,169	2.70	23,672	4.93	24,804	9.95
	2	44,348	45,545	2.70	46,534	4.93	48,760	9.95
1	0	8554	8785	2.70	8976	4.93	9405	9.95
	1	23,266	23,894	2.70	24,413	4.93	25,580	9.95
	2	45,224	46,445	2.70	47,453	4.93	49,722	9.95
2	0	10,157	10,432	2.71	10,659	4.93	11,168	9.95
	1	25,613	26,305	2.70	26,877	4.93	28,162	9.95
	2	48,007	49,303	2.70	50,374	4.93	52,783	9.95
IPT-based model ($r_0/h = 60$)								
0	0	2681	2748	2.49	2804	4.57	2930	9.25
	1	7302	7465	2.24	7604	4.14	7918	8.44
	2	14,069	14,339	1.92	14,577	3.61	15,116	7.45
1	0	2808	2878	2.47	2936	4.53	3066	9.19
	1	7523	7690	2.22	7833	4.12	8154	8.39
	2	14,334	14,608	1.91	14,849	3.60	15,396	7.41
2	0	3331	3412	2.45	3481	4.50	3635	9.13
	1	8267	8449	2.20	8604	4.07	8955	8.32
	2	15,186	15,472	1.88	15,725	3.55	16,299	7.34
IPT-based model ($r_0/h = 20$)								
0	0	7297	7384	1.19	7471	2.37	7670	5.10
	1	18,204	18,209	0.03	18,287	0.46	18,512	1.69
	2	32,172	31,892	−0.87	31,855	−0.99	31,924	−0.77
1	0	7607	7695	1.15	7783	2.31	7989	5.02
	1	18,738	18,746	0.04	18,829	0.48	19,069	1.76
	2	32,771	32,490	−0.86	32,457	−0.96	32,537	−0.72
2	0	9025	9130	1.16	9237	2.34	9486	5.11
	1	20,594	20,607	0.06	20,703	0.53	20,982	1.88
	2	34,711	34,418	−0.84	34,389	−0.93	34,492	−0.63

p = Number of nodal diameters, n = number of nodal circles.

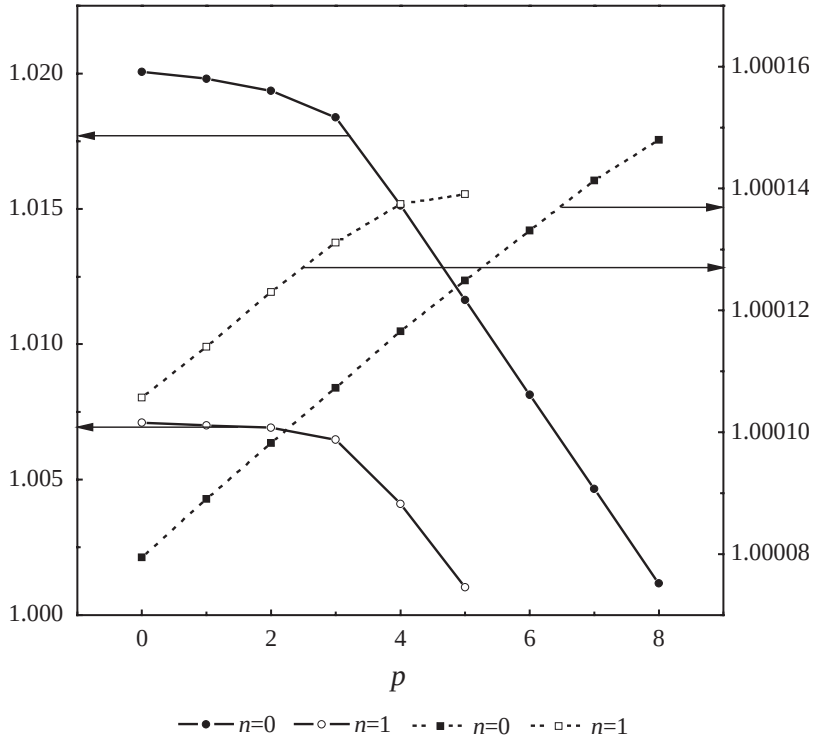

p= number of nodal diameters. n = number of nodal circles.

Fig. 3. Frequency ratio based on FEM simulation under C–C conditions (full line [left axis] — piezoelectric coupled plate with $r_0/h = 60$ and $h_1/2h = 1/10$ not accounting for piezoelectric effect over plate with piezoelectric layer removed ($h_1 = 0$); dotted line [right axis] — piezoelectric coupled plate accounting for piezoelectric effect over same plate without piezoelectric effect).

References

[1] H.J. Ding, B. Chen, J. Liang, General solutions for coupled equations for piezoelectric media, *International Journal of Solids and Structures* 33 (1996) 2283–2298.
[2] W.Q. Chen, Coupled Free Vibration of Spherically Isotropic Hollow Sphere, PhD Dissertation, Zhejiang University, Hangzhou, 1995.
[3] C.T. Sun, X.D. Zhang, Use of thickness-shear mode in constructing adaptive sandwich, *Smart Materials and Structures* 4 (1995) 202–206.
[4] X.D. Zhang, C.T. Sun, Analysis of sandwich plate containing a piezoelectric core, *Smart Materials and Structures* 8 (1999) 31–40.
[5] N. Sungsoo, L. Libresco, Oscillation control of cantilevers via smart materials technology and optimal feedback control: actuator location and power consumption issues, *Smart Materials and Structures* 7 (1998) 833–842.
[6] J.H. Han, L. Lee, Analysis of composite plates with piezoelectric actuators for vibration control using layerwise displacement theory, *Composites B* 29 (1998) 621–632.
[7] Q. Wang, S.T. Quek, C.T. Sun, X. Liu, Analysis of piezoelectric coupled circular plate, *Smart Materials and Structures* 10 (2001) 229–239.
[8] X. Liu, Q. Wang, S.T. Quek, Analytical solution for free vibration of piezoelectric coupled moderately thick circular plates, *International Journal of Solids and Structures* 39 (2002) 2129–2151.

[9] K. Uchino, Piezoelectric ultrasonic motors: overview, *Smart Materials and Structures* 7 (1998) 273–285.
[10] T.A. Takano, H. Hirata, Y. Tomikawa, Analysis of non-axisymmetric vibration mode piezoelectric annular plate and its application to an ultrasonic motor, *IEEE Transactions on Ultrasonics, Ferroelectrics and Frequency Control* 37 (1990) 558–565.
[11] P. Hagedorn, J. Wallashek, Traveling wave ultrasonic motors—part II: working principle and mathematical modeling of the stator, *Journal of Sound and Vibration* 155 (1992) 31–46.
[12] M. Yang, P. Que, Performances estimation of a rotary traveling wave ultrasonic motor based on two-dimension analytical model, *Ultrasonics* 39 (2001) 115–120.
[13] J.R. Friend, D.S. Stutts, The dynamics of an annular piezoelectric motor stator, *Journal of Sound and Vibration* 204 (1997) 421–437.
[14] N.W. Hagood, A.J. McFarland, Modeling of a piezoelectric rotary ultrasonic motor, *IEEE Transactions on Ultrasonics, Ferroelectrics and Frequency Control* 42 (1995) 210–224.
[15] R.D. Mindlin, Influence of rotary inertia and shear on flexural motions of isotropic, elastic plates, *Journal of Applied Mechanics* 18 (1951) 31–38.
[16] R.D. Mindlin, H.D. Medick, Extensional vibrations of elastic plates, *Journal of Applied Mechanics* 26 (1959) 561–569.